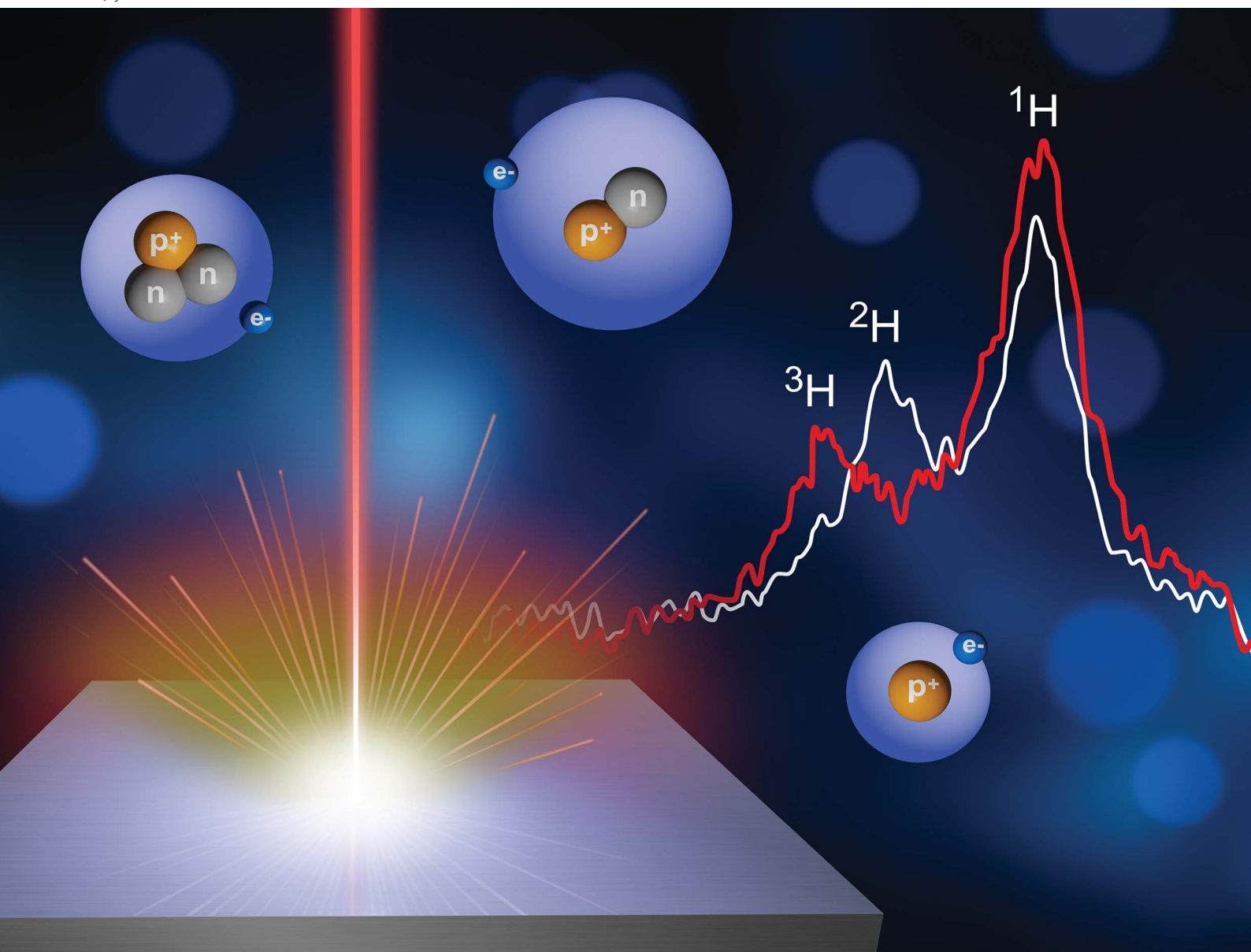


JAAS

Journal of Analytical Atomic Spectrometry

rsc.li/jaas



ISSN 0267-9477

COMMUNICATION

Sivanandan S. Harilal *et al.*
Detection of tritium using ultrafast laser-induced breakdown
spectroscopy



Cite this: *J. Anal. At. Spectrom.*, 2024, **39**, 699

Received 8th December 2023
Accepted 1st February 2024

DOI: 10.1039/d3ja00439b

rsc.li/jaas

Detection of tritium using ultrafast laser-induced breakdown spectroscopy

Sivanandan S. Harilal,^{ID}*^a Abdul K. Shaik,^a Elizabeth J. Kautz,^{ID}^{ab} Arun Devaraj,^{ID}^a Andrew M. Casella^a and David J. Senor^a

Detection of nuclear materials and their radioisotopes with rapid, and standoff capability in addition to no sample preparation requirement is crucial to nuclear nonproliferation, safeguards, and security. In this work, we demonstrate the first application of ultrafast laser-induced breakdown spectroscopy to detect tritium (^3H) during depth profiling of neutron-irradiated Zircaloy-4 samples.

Detection of radioactive nuclear materials and their isotopes is very important in numerous fields including nuclear nonproliferation, treaty verification, nuclear security, safeguards, fuel fabrication, and forensics.^{1,2} Some of the key required attributes for nuclear material detection for field analysis are rapid and non-contact detection with minimal to no sample preparation. Currently, mass spectrometry tools such as inductively coupled plasma mass spectrometry (ICP-MS), secondary ion mass spectrometry (SIMS), thermal ion mass spectrometry (TIMS), and atom probe tomography (APT) are regularly used for detecting U, Pu, H, Li and their isotopes.^{3–5} However, all of these techniques are laboratory-based and require extensive sample preparation. Mass spectrometry methods such as ICP-MS are capable of high precision measurements,⁶ whereas other instruments, *e.g.*, nanoscale SIMS⁷ and APT,⁵ can map isotopes with nanometer-scale spatial resolution. Some of these techniques are not useful for obtaining spatial information (*e.g.*, ICP-MS). On the other hand, although the high spatial resolution is possible with NanoSIMS or APT methods, they are not capable of surveying large sample areas that may be needed for post-irradiation examinations of fuel rods or tritium-producing burnable absorber rod (TPBAR) components.⁸

Optical spectroscopic tools (*e.g.*, emission, absorption, and laser-induced fluorescence) can detect all nuclear materials and some of their isotopes, offering rapid, non-contact analytical capability of solid material when combined with laser

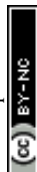
ablation.^{2,9} Among these optical methods, laser-induced breakdown spectroscopy (LIBS) is most frequently used for isotopic analysis because of its non-intrusive nature and rapid in-field use.^{10–13} So far, LIBS has been successfully demonstrated for discriminating various nuclear-related materials isotopes such as U ($^{235}\text{U}/^{238}\text{U}$),^{2,10} Pu ($^{239}\text{Pu}/^{240}\text{Pu}$),^{14,15} Li ($^6\text{Li}/^7\text{Li}$),^{12,16} and H ($^1\text{H}/^2\text{H}$).^{17–20} LIBS has the ability to provide spatially resolved maps of H isotopes and perform depth profiling. In particular, when an ultrafast laser is used for ablation, improved spatial mapping and precision depth profiling capabilities can result, owing to its limited heat-affected zone in comparison to nano-second pulsed lasers.^{2,21}

One of the challenges associated with LIBS for isotopic analysis of light elements is the line broadening. LIBS requires thermal excitation which happens only at early times of laser-produced plasma evolution where various plasma broadening mechanisms dominate. In addition, the spectral resolution of an emission spectroscopy system is inherently limited by the instrumental broadening of the spectrograph. Although the isotopic shifts/splitting (IS) of the H_α (656.28 nm) is relatively large ($^1\text{H}_\alpha - ^2\text{H}_\alpha \approx 180$ pm, $^1\text{H}_\alpha - ^3\text{H}_\alpha \approx 240$ pm) compared to transitions of other elements, the H_α emission from the plasma is inherently broadened because of its linear Stark effect. Being the lightest element in the periodic table, there should be significant Doppler broadening too in H transitions. Previous studies highlighted that a flowing inert-gas (*e.g.*, Ar, He) and reduced pressure environment (≈ 10 –50 Torr) provided good signal-to-noise ratios and narrower linewidths for H isotopic analysis.^{11,22}

Tritium (^3H) is a radioactive isotope of hydrogen that is used in a wide variety of applications, particularly as a fuel in fusion reactors, and in nuclear devices.²³ Given the toxicity of ^3H to humans and the environment, standoff sensing methods are needed, which becomes increasingly important in the context of post-irradiation examinations in which contact with radioactive materials should be minimized. ^3H has a low natural abundance and therefore is produced *via* neutron irradiation of lithium-bearing pellets in nuclear reactors according to the

^aPacific Northwest National Laboratory, Richland, Washington 99354, USA. E-mail: hari@pnnl.gov

^bNuclear Engineering Department, North Carolina State University, Raleigh, North Carolina 27695, USA



following reaction: ${}^6\text{Li} + \text{n} \rightarrow {}^4\text{He} + {}^3\text{H}$. The ${}^3\text{H}$ then diffuses through the pellet to a surrounding Zircaloy-4 tube that acts as a ${}^3\text{H}$ getter.⁸ Measurement of ${}^3\text{H}$ stored in the getter using rapid, standoff methods would greatly enhance understanding of ${}^3\text{H}$ produced during irradiation, and its distribution along the length and through the thickness of the getter material. In this work, we report the detection of ${}^1\text{H}$, ${}^2\text{H}$, and ${}^3\text{H}$ from ${}^2\text{H}$ -loaded (*i.e.*, deuterated) and neutron-irradiated Zircaloy-4 using ultrafast LIBS. ${}^2\text{H}$ -loaded Zircaloy-4 samples were used for the initial optimization experiments, while ${}^3\text{H}$ in the Zircaloy was monitored/detected using ultrafast LIBS *via* depth profiling.

The LIBS experiments were carried out using pulses from a Ti:Sapphire laser (800 nm, ≈ 35 fs pulse duration, maximum energy ≈ 7 mJ). The laser was operated at 5 Hz. The spot size at the target was kept at ≈ 65 μm in diameter. The laser energy was attenuated using a combination of a half-wave plate and a thin-film polarizer. Two different cubic vacuum chambers ($6 \times 6 \times 6$ inches³) with identical features were used in the present experiment: (1) for experiments employing ${}^2\text{H}$ -loaded Zircaloy-4, and (2) for irradiated samples because of the radiological safety constraints. Both chambers contained a pressure gauge, vacuum pump, and gas lines for controlling the gas environment and pressure in addition to optical windows for laser entrance and light collection. Initial experiments were carried out on a ${}^2\text{H}$ -loaded Zircaloy-4 sample with ≈ 4300 ppm ${}^2\text{H}$ to understand the impact of environmental parameters, such as ambient gas pressure and oxygen chemistry on optical signatures. The ${}^2\text{H}$ -loaded sample was prepared using a custom-built high vacuum system, details of which are provided in our prior work.²² Spatially and depth-wise uniformity of ${}^2\text{H}$ loading was noted in these samples. For ${}^3\text{H}$ detection and analysis, a neutron-irradiated Ni-coated Zircaloy-4 sample was used. Neutron irradiation was carried out at the Watts Bar Nuclear Power Plant. The measured dose of the irradiated Zircaloy-4 sample prior to analysis was 11 mR at contact and 0.6 mR at 6 inches. Since neutron flux is expected to vary with space in a reactor,²⁴ the ${}^3\text{H}$ production and absorption in the Zircaloy-4 getter sample is also expected to vary spatially as well as with depth. Both ${}^2\text{H}$ -loaded and irradiated samples are cylindrical rods.

The samples were positioned in the center of the vacuum chamber which was pumped using a rotary pump to a base pressure of 100 mTorr. The chamber was positioned on an *x-y* translator to provide a fresh target surface for ablation. Ar was used as the buffer gas. The pressure inside the chamber containing the ${}^2\text{H}$ -loaded sample was varied to evaluate the optimal conditions of H isotope detection, and ablation depth/pulse. The chamber containing the irradiated sample was pumped down to 100 mTorr and then backfilled with argon to 45 Torr and the ambient environment was kept static during all data collection.

Spatially integrated, and time-resolved emission features were analyzed using a 0.75 m spectrograph consisting of 2400 grooves per mm grating (Spectrapro HRS-750, Princeton Instruments) and an intensified CCD (ICCD) as the detector (PIMAX4, Princeton Instruments). The measured spectral resolution at 632.8 nm using a He-Ne laser was ≈ 13 pm at full

width half maximum (FWHM). The thermal emission from the plasma was collected near normal to the target using a plano-convex lens and focused onto a fiber bundle for light transport. For evaluating the plasma dynamics and drilling, an ICCD positioned orthogonal to the plasma expansion direction was used and time-resolved images of the plasma plumes were collected.

In the present work, due to radiological safety concerns associated with ${}^3\text{H}$, the LIBS measurements of irradiated samples were conducted in a static background pressure. Hence any presence of oxygen in the chamber (due to leakage or presence of H_2O) may influence the analytical merits of ${}^3\text{H}$ detection. So, the initial experiments were carried out using ${}^2\text{H}$ -loaded Zircaloy-4 samples to understand the ambient pressure effects on signal intensity, linewidth, and the role of oxygen presence on H isotopic emission signatures.

Typical spectral features from deuterated Zircaloy-4 plasma at various Ar pressures in the spectral range 655–658 nm are given in Fig. 1. The prominent emission lines in the spectra are ${}^2\text{H}_\alpha$ at 656.10 nm, ${}^1\text{H}_\alpha$ at 656.28 nm, Zr I at 656.95 nm and Zr I at 657.66 nm.²⁵ The measurements were taken using a gate delay of 1 μs and with a gate width of 3 μs . The spectral features clearly show that at higher pressure, the ${}^1\text{H}_\alpha$ and ${}^2\text{H}_\alpha$ lines are partially resolved, and the isotopic resolution (peak separation) improves at reduced pressure. The presence of ${}^1\text{H}$ in the spectral features is partly contributed by contamination on the

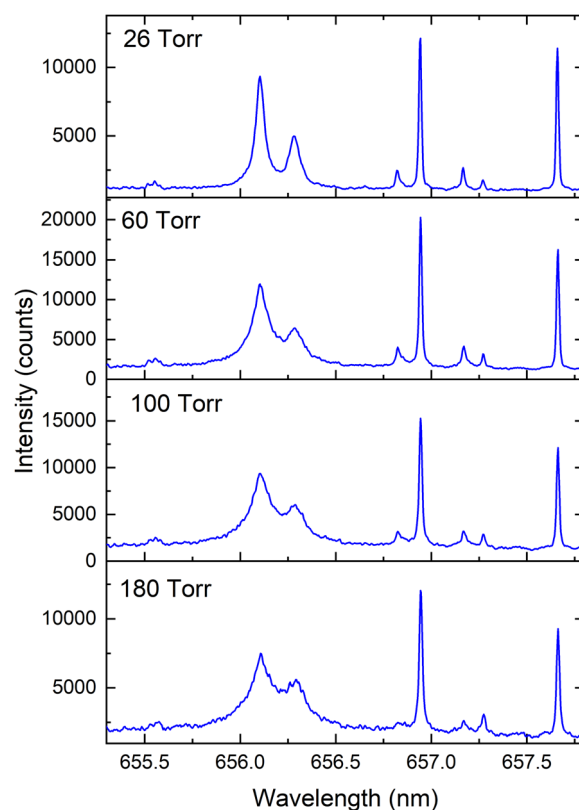


Fig. 1 Spectral emission features from Zircaloy-4 sample showing ${}^2\text{H}_\alpha$ and ${}^1\text{H}_\alpha$ transitions at various Ar background pressure levels. Additional lines seen in the spectra are contributed by Zr I. The detection delay time and gate width used were 1 μs /3 μs .



sample surface and from the environment. The measured intensity of the $^2\text{H}_\alpha$ line along with its FWHM is provided in Fig. 2 which shows that $^2\text{H}_\alpha$ emission intensity peaks at ≈ 20 –50 Torr Ar pressure levels. The linewidth, which is one of the most important considerations for isotopic analysis using optical spectroscopy, increases with pressure because of the plume confinement.²⁶ The FWHMs of ^2H and ^1H are significantly broadened compared to Zr I transitions seen in Fig. 1. For example, at 26 Torr pressure, the measured FWHM of Zr I transition is near the instrumental limit while the linewidth of $^2\text{H}_\alpha \approx 80$ pm. Since the emission from H and its isotopes peaks at early times of plasma evolution due to its very high upper energy level (≈ 12.3 eV), it is difficult to avoid the linear Stark contribution caused by the higher LPP electron density. Being the lightest element, the Doppler effect is also significant for H and its isotopes. For example, for a plasma with a $1 \times 10^{15} \text{ cm}^{-3}$ density and a temperature of 4000 K, the estimated linewidths caused by Stark and Doppler effects are ≈ 15 pm. In addition, fine spectral components are present in the $^1\text{H}_\alpha$ and $^2\text{H}_\alpha$ lines which span ≈ 20 pm.²⁵

Fig. 2 also shows that the pressure of the ambient medium has opposing effects on $^2\text{H}_\alpha$ signal levels and FWHM values when the background pressure is ≥ 30 Torr (*i.e.*, intensity decreases, and FWHM increases). These trends highlight important trade-offs in the LIBS analysis of H and its isotopes, and that reduced pressures are optimal for achieving strong emission signals with reduced line broadening. The intensity and linewidth changes with pressure provided in Fig. 2 were also carried out when the inert gas flowed through the chamber rather than in static conditions. However, our studies also showed that a flowing inert gas environment provided a higher emission intensity of $^2\text{H}_\alpha$ instead of a static gas environment. Hence, a study has been carried out to evaluate the role of trace oxygen in the chamber on $^1\text{H}_\alpha$ and $^2\text{H}_\alpha$ emission intensities.

Fig. 3 reports changes in $^2\text{H}_\alpha$ and $^1\text{H}_\alpha$ emission intensities with the addition of air partial pressures to the chamber containing 35 Torr Ar, and it clearly shows that the increasing

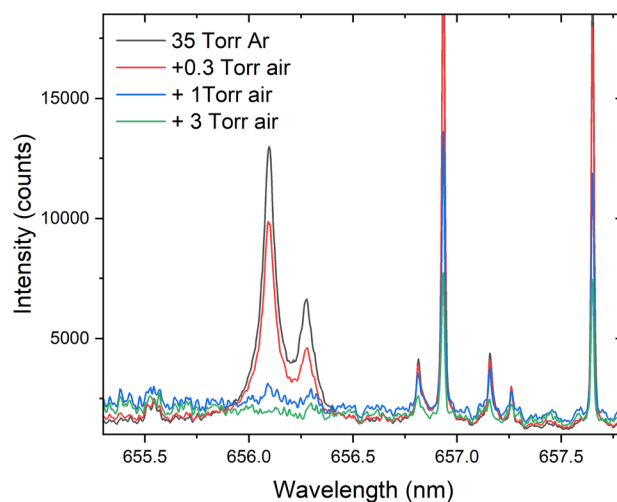


Fig. 3 The changes in $^1\text{H}_\alpha$ and $^2\text{H}_\alpha$ intensity with the addition of partial pressures of air into 35 Torr Ar.

presence of oxygen partial pressure in the chamber deteriorates the $^2\text{H}_\alpha$ and $^1\text{H}_\alpha$ signal intensities. For example, with the addition of ≈ 300 mTorr of oxygen to the chamber, the $^2\text{H}_\alpha$ signal intensity reduced drastically. The presence of oxygen in the chamber may initiate plasma chemical reactions that lead to the formation of molecular species (OH and OD), affecting the analytical merits of the H isotopic emission signal. Previous studies employing U also showed similar trends (reduction of U I with the formation of UO and higher oxides).²⁷

Ultrafast laser depth profiling of the deuterated Zircaloy-4 sample was carried out to estimate ablation depth per pulse using gated plasma imaging.²⁸ Images were collected by positioning an ICCD orthogonal to the plasma expansion direction and by monitoring the emission from the outer and inner surfaces of the cylindrical target. The laser energy and laser spot size used were ≈ 5.3 mJ and ≈ 65 μm . The emission from the inner surface of the cylinder appeared after 88 laser shots, indicating the presence of a drilled-thru hole. Assuming constant ablation depth per pulse, the estimated ablation efficiency of the Zircaloy target is ≈ 2 μm per pulse.

Considering ^3H is toxic and volatile, the LIBS measurements of irradiated samples were all carried out in a static 45 Torr Ar environment. The ^3H studied here was produced *via* neutron irradiation of a ^6Li -enriched LiAlO_2 ceramic pellet which was surrounded by a Zircaloy-4 tube that acts as a ^3H getter. This Zircaloy-4 getter component is Ni-plated to prevent oxidation.⁸ Hence, a depth profiling study is required to detect ^3H in the irradiated Zircaloy-4 getter target. An example of the measurement of $^3\text{H}_\alpha$ during depth profiling is given in Fig. 4. The ^3H signal was not evident at shallow depths where $^1\text{H}_\alpha$ signal predominates. The $^3\text{H}_\alpha$ signal was more prominent when the number of laser shots at the target reached ≥ 40 during depth profiling. Then, the relative intensity of $^3\text{H}_\alpha$ vs. $^1\text{H}_\alpha$ increased with the increasing number of laser shots. The signal levels dropped significantly after 80 laser shots. We also noticed the $^3\text{H}_\alpha$ signal intensity varies significantly at various locations in the irradiated target. The strong presence of $^1\text{H}_\alpha$ in the

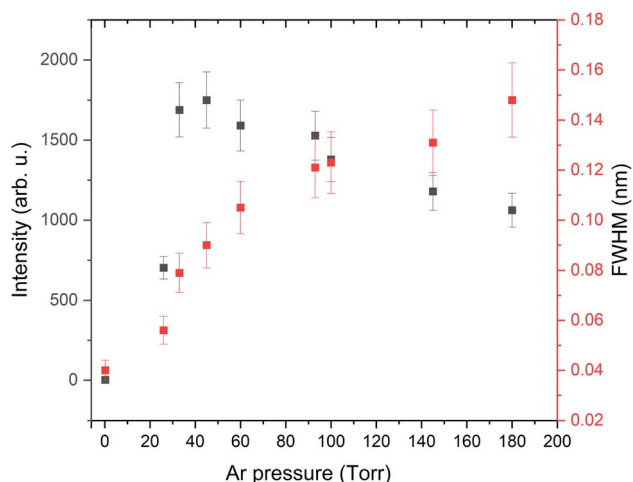


Fig. 2 $^2\text{H}_\alpha$ emission intensity (black squares) and FWHM (red squares) from deuterated Zircaloy plasma at various Ar pressure levels.



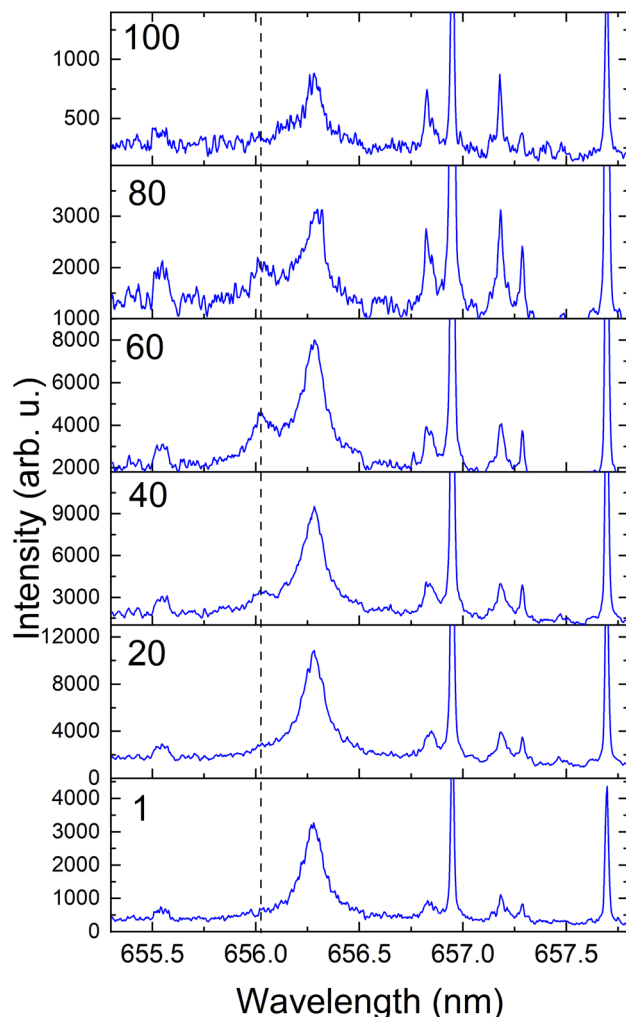


Fig. 4 Emission spectra from irradiated Zircaloy-4 during fs laser depth profiling. The numbers given in the figures correspond to the beginning number of laser shots during the depth profiling. The dotted line represents the spectral position of the ^3H peak. The ^3H peak appears after 40 laser shots. Each spectrum is averaged over 10 laser shots.

irradiated target is due to ingress through the TPBAR stainless steel cladding from the reactor coolant along with contamination.⁸

According to the present results, the ^3H distribution in the Zircaloy getter sample was highly localized. The lack of ^3H on the top of the surface can be attributed to the Ni-plating, which was used to prevent the oxidation of Zircaloy-4 surfaces during irradiation in a light-water reactor. Considering the nonuniform neutron flux in the reactor, it can be anticipated that the ^3H deposition of the irradiated Zircaloy-4 getter sample could vary significantly along the surface and depth-wise due to the dynamic environment inside nuclear reactors. In addition, the permeation of ^3H into the grain boundaries, the decay of the generated ^3H , and the discrete nature of the hydrides in the Zircaloy may also contribute to nonuniform ^3H concentration in the sample.^{29,30}

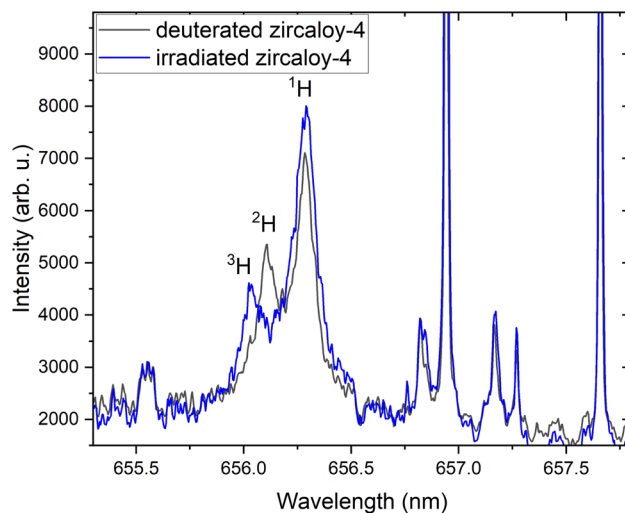


Fig. 5 Comparison of emission signatures from deuterated and irradiated Zircaloy-4 samples showing all hydrogen isotopic peaks.

Fig. 5 compares emission signatures from deuterated and irradiated Zircaloy-4 samples. The measured spectral positions of ^1H , ^2H , and ^3H are 656.28 nm, 656.1 nm, and 658.03 nm, respectively. Since the spectral measurements given in Fig. 5 were carried out in 45 Torr Ar background pressure, significant spectral broadening can be seen and it may hinder measuring smaller isotopic splitting of $^2\text{H}_\alpha$ - $^3\text{H}_\alpha$ compared to $^1\text{H}_\alpha$ - $^3\text{H}_\alpha$ or $^1\text{H}_\alpha$ - $^2\text{H}_\alpha$ isotopic splitting. It indicates that a reduced background pressure environment that provides narrower line-widths (see Fig. 2) is necessary for analyzing $^2\text{H}_\alpha$ - $^3\text{H}_\alpha$ isotopic splitting.

In summary, we report the first demonstration of ^3H detection using ultrafast LIBS. We monitored ^1H , ^2H , and ^3H during depth profiling of deuterated and neutron-irradiated Zircaloy-4 samples. The ^3H distribution in the Zircaloy sample was highly localized and well-resolved isotopic peaks were detected during depth profiling of irradiated targets. The present study highlights the successful use of ultrafast LIBS for the rapid detection of ^3H with no sample preparation, with additional capabilities of spatial mapping and depth profiling.

Conflicts of interest

There are no conflicts to declare.

Acknowledgements

This work was supported by the DOE/NNSA Tritium Modernization Program. The authors thank Ingrid Burgeson, Emily Campbell, and Ewa Ronnebro for arranging the samples, and PNNL's radiological protection technologists for their support. Pacific Northwest National Laboratory is a multi-program national laboratory operated by Battelle for the U.S. Department of Energy under Contract DE-AC05-76RL01830.



Notes and references

- 1 D. LaGraffe, *Handbook of Security Science*, Springer, 2022, pp. 795–827.
- 2 S. S. Harilal, B. E. Brumfield, N. L. LaHaye, K. C. Hartig and M. C. Phillips, *Appl. Phys. Rev.*, 2018, **5**, 021301.
- 3 S. Evers, C. Senöz and M. Rohwerder, *Sci. Technol. Adv. Mater.*, 2013, **14**, 014201.
- 4 Y.-S. Chen, P.-Y. Liu, R. Niu, A. Devaraj, H.-W. Yen, R. K. Marceau and J. M. Cairney, *Microsc. Microanal.*, 2023, **29**, 1–15.
- 5 A. Devaraj, B. Matthews, B. Arey, L. Bagaasen, E. Buck, G. Sevigny and D. Senor, *Mater. Charact.*, 2021, **176**, 111095.
- 6 G. Galbács, A. Kéri, I. Kálomista, É. Kovács-Széles and I. B. Gornushkin, *Anal. Chim. Acta*, 2020, **1104**, 28–37.
- 7 K. Li, J. Liu, C. R. Grovenor and K. L. Moore, *Annu. Rev. Anal. Chem.*, 2020, **13**, 273–292.
- 8 K. A. Burns, E. F. Love and C. K. Thornhill, *Description of the Tritium-Producing Burnable Absorber Rod for the Commercial Light Water Reactor*, Pacific Northwest National Laboratory report, PNNL-22086 technical report, 2012.
- 9 E. J. Kautz, M. C. Phillips and S. S. Harilal, *J. Appl. Phys.*, 2021, **130**, 203302.
- 10 D. A. Cremers, A. Beddingfield, R. Smithwick, R. C. Chinni, C. R. Jones, B. Beardsley and L. Karch, *Appl. Spectrosc.*, 2012, **66**, 250–261.
- 11 E. J. Kautz, A. Devaraj, D. J. Senor and S. S. Harilal, *Opt. Express*, 2021, **29**, 4936–4946.
- 12 E. J. Kautz, A. Xu, A. V. Harilal, M. P. Polek, A. M. Casella, D. J. Senor and S. S. Harilal, *Opt. Express*, 2023, **31**, 3549–3564.
- 13 J. Wu, Y. Qiu, X. Li, H. Yu, Z. Zhang and A. Qiu, *J. Phys. D: Appl. Phys.*, 2019, **53**, 023001.
- 14 C. A. Smith, M. A. Martinez, D. K. Veirs and D. A. Cremers, *Spectrochim. Acta, Part B*, 2002, **57**, 929–937.
- 15 S. S. Harilal, C. M. Muryzn, E. J. Kautz, M. K. Edwards, S. I. Sinkov, S. S. Bisson and J. B. Martin, *J. Anal. At. Spectrom.*, 2021, **36**, 150–156.
- 16 J. C. Wood and M. B. Shattan, *Appl. Spectrosc.*, 2021, **75**, 199–207.
- 17 M. Burger, P. Skrodzki, L. Finney, J. Hermann, J. Nees and I. Jovanovic, *Phys. Plasmas*, 2018, **25**, 083115.
- 18 R. Fantoni, S. Almaviva, L. Caneve, F. Colao, G. Maddaluno, P. Gasior and M. Kubkowska, *Spectrochim. Acta, Part B*, 2017, **129**, 8–13.
- 19 E. J. Kautz, D. J. Senor and S. S. Harilal, *J. Appl. Phys.*, 2021, **130**, 204901.
- 20 K. H. Kurniawan, M. O. Tjia and K. Kagawa, *Appl. Spectrosc. Rev.*, 2014, **49**, 323–434.
- 21 V. Gardette, V. Motto-Ros, C. Alvarez-Llamas, L. Sancey, L. Duponchel and B. Busser, *Anal. Chem.*, 2023, **95**, 49–69.
- 22 E. J. Kautz, E. Ronnebro, A. Devaraj, D. Senor and S. S. Harilal, *J. Anal. At. Spectrom.*, 2021, **36**, 1217.
- 23 H. Van Der Meiden, S. Almaviva, J. Butikova, V. Dwivedi, P. Gasior, W. Gromelski, A. Hakola, X. Jiang, I. Jögi, J. Karhunen, et al., *Nucl. Fusion*, 2021, **61**, 125001.
- 24 B. Van der Ende, L. Li, D. Godin and B. Sur, *Nat. Commun.*, 2019, **10**, 1959.
- 25 A. Kramida, Yu. Ralchenko, J. Reader and NIST ASD Team, *NIST Atomic Spectra Database (Ver. 5.9)*, National Institute of Standards and Technology, Gaithersburg, MD, 2021, available: <https://physics.nist.gov/asd>.
- 26 S. Harilal, C. Bindhu, M. Tillack, F. Najmabadi and A. Gaeris, *J. Appl. Phys.*, 2003, **93**, 2380–2388.
- 27 E. J. Kautz, E. N. Weerakkody, M. S. Finko, D. Curreli, B. Koroglu, T. P. Rose, D. G. Weisz, J. C. Crowhurst, H. B. Radousky, M. DeMagistris, et al., *Spectrochim. Acta, Part B*, 2021, **185**, 106283.
- 28 S. Harilal, M. Phillips, D. Froula, K. Anoop, R. Issac and F. Beg, *Rev. Mod. Phys.*, 2022, **94**, 035002.
- 29 A. T. Motta, L. Capolungo, L.-Q. Chen, M. N. Cinbiz, M. R. Daymond, D. A. Koss, E. Lacroix, G. Pastore, P.-C. A. Simon, M. R. Tonks, et al., *J. Nucl. Mater.*, 2019, **518**, 440–460.
- 30 J. Bair, M. A. Zaeem and M. Tonks, *J. Nucl. Mater.*, 2015, **466**, 12–20.

